

A CHANDRA STUDY OF TEMPERATURE SUBSTRUCTURES IN INTERMEDIATE-REDSHIFT GALAXY CLUSTERS

Liyi Gu¹, Haiguang Xu¹, Junhua Gu¹, Yu Wang¹, Zhongli Zhang², Jingying Wang¹,
Zhenzhen Qin¹, Haijuan Cui¹, Xiang-Ping Wu³

ABSTRACT

By analyzing the gas temperature maps created from the *Chandra* archive data, we reveal the prevailing existence of temperature substructures on $\sim 100 h_{70}^{-1}$ kpc scales in the central regions of nine intermediate-redshift ($z \approx 0.1$) galaxy clusters, which resemble those found in the Virgo and Coma Clusters. Each substructure contains a clump of hot plasma whose temperature is about 2 – 3 keV higher than the environment, corresponding to an excess thermal energy of $\sim 10^{58-60}$ erg per clump. Since if there were no significant non-gravitational heating sources, these substructures would have perished in 10^{8-9} yrs due to thermal conduction and turbulent flows, whose velocity is found to range from about 200 to 400 km s⁻¹, we conclude that the substructures cannot be created and sustained by inhomogeneous radiative cooling. We also eliminate the possibilities that the temperature substructures are caused by supernova explosions, or by the non-thermal X-ray emission due to the inverse-Comptonization of the CMB photons. By calculating the rising time of AGN-induced buoyant bubbles, we speculate that the intermittent AGN outbursts ($\geq 10^{60}$ erg per burst) may have played a crucial role in the forming of the high temperature substructures. Our results are supported by recent study of McNamara & Nulsen (2007), posing a tight observational constraint on future theoretical and numerical studies.

Subject headings: galaxies: clusters: general — galaxies: intergalactic medium
— techniques: image processing — X-rays: galaxies: clusters

¹Department of Physics, Shanghai Jiao Tong University, 800 Dongchuan Road, Shanghai 200240, PRC

²Max-Planck-Institut für extraterrestrische Physik, Giessenbachstraße, 85748 Garching, Germany

³National Astronomical Observatories, Chinese Academy of Sciences, 20A Datun Road, Beijing 100012, PRC

1. INTRODUCTION

In the frame of hierarchical formation theories, it is believed that the mass clustering develops due to the gravitational instability caused by the intrinsic, tiny Gaussian density perturbations that existed in the early universe (see, e.g., Frenk et al. 1996 for a review). Since the initial conditions and input physics are assumed to be scale-free, dark halos are expected to have evolved self-similarly in time, which can be described by the scaling laws over many fundamental parameters (Navarro et al. 1995 and references therein), as have been advocated by the numerical simulations in which spherical collapse and adiabatic gas dynamics are assumed (e.g., Navarro et al. 1996; Eke et al. 1998).

On the observational aspect, tight correlations between X-ray luminosity, gas temperature, gas entropy, X-ray isophotal radius, and virial mass of galaxy clusters have been discovered successively with *Einstein*, *ASCA*, and *ROSAT* (e.g., Mushotzky 1984; Mohr & Evrard 1997; Horner et al. 1999). These correlations, however, often show notable deviations from theoretical predictions. For example, in early 1990s, a significant scatter on the measured luminosity-temperature curves was reported by, e.g., Edge & Stewart (1991) and Fabian et al. (1994b), who showed that the cool-core galaxy clusters are more luminous at a given temperature. The observed mass-temperature relation, on the other hand, shows a lower ($\sim 40\%$) normalization and a steeper slope with respect to the prediction of adiabatic models (e.g., Evrard et al. 1996; Xu et al. 2001). Moreover, an excess in the gas entropy was found in the central regions ($< 0.05R_{200}$) of many low temperature systems (Ponman et al. 1999, 2003), which forms a platform of extra energy ($\sim 1 - 3$ keV per particle; Tozzi & Norman 2001) on the entropy-temperature curve. These deviations and mismatches, which have been confirmed with *Chandra* and *XMM-Newton* observations recently (e.g., Arnaud et al. 2005; Kotov & Vikhlinin 2006), clearly indicate that our understanding of the thermal history of galaxy clusters is far from complete, and the roles played by non-gravitational heating processes need to be evaluated properly (e.g., Kaiser 1991; Evrard & Henry 1991; Kauffmann et al. 1993), which will also help solve the cooling flow problem (Fabian 1994a; Makishima et al. 2001; Peterson et al. 2003).

As of today, a number of heating sources have been proposed, which include merger shocks, cosmic rays, supernovae, thermal conduction, turbulent dissipation and diffusion, and AGN feedbacks (e.g., McNamara & Nulsen 2007; Markevitch & Vikhlinin 2007). However, none of the proposed candidates is all-purpose for halting the gas cooling and breaking the self-similarities on both galactic and cluster scales. For example, recent observations (e.g., Croston et al. 2005; Jetha et al. 2007) showed that, AGN activity, the most representative heating source of today, tends to deposit most of its energy into the vast intergalactic space, rather than within the host galaxy ($< 0.05R_{500}$). Clearly, detailed mappings of gas

temperature gradients in the ICM is necessary as a crucial observational constraint in order to correctly investigate the gas heating history.

Two-dimensional gas temperature variations have been observed in many galaxy clusters with *Chandra* and *XMM-Newton*. By analyzing the temperature map generated with the high-quality *Chandra* data, Fabian et al. (2000) identified a pair of cool gas shells that coincide with two radio bubbles, whose radii are ~ 6 and $8 h_{70}^{-1}$ kpc, respectively, in the innermost region of the Perseus Cluster. The authors suggested that the cool gas shells were formed as the buoyant gas detached from the terminals of AGN jets and inflated in pressure equilibrium with the surrounding gas. Similar phenomenon was also observed in, e.g., Centaurus cluster (Fabian et al. 2005), Abell 2052 (Blanton et al. 2003), and Hydra A (Nulsen et al. 2002). Also, in clusters that show clear merger signatures, such as 1E 0657-56 (Govoni et al. 2004), Abell 3667 (Vikhlinin et al. 2001), Abell 665, and Abell 2163 (Markevitch & Vikhlinin 2001), conspicuous temperature variations were copiously found, which are presumably caused by the rapid adiabatic expansion of the shock-heated gas.

So far, however, in most of the existing works, little has been done to measure the morphologies of the temperature substructures and to investigate their origins in a quantitative way. One of few exceptional works was presented by Shibata et al. (2001), who calculated the two point correlation function of the *ASCA* hardness ratio map of the Virgo Cluster, and found that there is a characteristic scale of $\sim 300 h_{70}^{-1}$ kpc for the two-dimensional temperature variations. The authors associated this characteristic scale with the size of the gas blobs arising during the infalling of sub-groups. By analyzing the two-dimensional temperature distribution with the *XMM-Newton* data, Schuecker et al. (2004) reported the presence of a turnover at $\sim 100 h_{70}^{-1}$ kpc on the pressure fluctuation spectrum of the Coma Cluster, and attributed it to the existence of Kolmogorov/Oboukhov-type turbulent flows. As of today, due to the lack of more such quantitative studies, it is not clear if there does exist a prevalence for a characteristic scale $\sim 100 h_{70}^{-1}$ kpc in galaxy clusters and groups, and how far it can be used to constrain the heating models in the ICM.

In this work we analyze the *Chandra* archive data to search for possible characteristic scales of temperature variations in a sample of nine intermediate-redshift clusters. In §2 & 3, we describe the sample selection criteria and data analysis, respectively. In §4, we discuss the physical implications of the results. In §5, we summarize our work. We assume $H_0 = 70$ km s^{-1} Mpc^{-1} , a flat universe for which $\Omega_0 = 0.3$ and $\Omega_\Lambda = 0.7$, and adopt the solar abundance standards of Grevesse & Sauval (1998).

2. SAMPLE AND DATA PREPARATION

In order to balance between the angular resolution and detector coverage of the targets, we construct our sample with nine intermediate-redshift ($z \simeq 0.1$) galaxy clusters, so that the central $400 h_{70}^{-1}$ kpc regions of the clusters can be fully, or nearly fully covered by the S3 CCD of the *Chandra* advanced CCD imaging spectrometer (ACIS) instrument. All the selected clusters have a $0.7 - 8.0$ keV flux greater than 5.0×10^{-12} erg s $^{-1}$ cm $^{-2}$. We list some basic properties of these clusters in Table 1, which are arranged in the orders of source names (col. [1]), names of the cD galaxies (col. [2]), redshifts (col. [3]), richness classes (col. [4]), right ascension and declination coordinates (J2000) of the cluster optical centroids (col. [5] & [6]), and notes (col. [7]).

On the optical and infrared images extracted from the DSS¹ (Fig. 1) and 2MASS² archives, we do not find any strong evidence for pronounced signatures caused by major mergers on cluster scales, such as off-center optical and/or infrared substructures. A478, A1068, A1650, A2244, and A3112 possess a central galaxy that has been classified as a cD, whose size is > 3 times that of any other member galaxy (Rood & Sastry 1971; Takizawa et al. 2003). The remaining four clusters are dominated by a pair or a clump of brightest member galaxies (Struble & Rood 1987). In addition, Schombert et al. (1989) reported the existence of a low-velocity (the radial velocity difference is $\Delta v_r \approx 50$ km s $^{-1}$) companion galaxy dwelling deep inside the envelope of the cD galaxy of A2244.

Strong radio emission associated with AGN activity has been detected in four clusters. In A478, two symmetric radio lobes are identified at 1.4 GHz, which extend about $3''$ towards northeast and southwest, respectively (Sun et al. 2003). In A1068, two compact radio sources are resolved, which are consistent with the locations of the cD galaxy and SDSS J104043.45+395705.3 (a member galaxy located at about $13''$ southwest of the cluster center), respectively (McNamara et al. 2004). A2204 and A3112 are reported to possess an extended radio halo that roughly traces the spatial distribution of the X-ray gas, respectively (Sanders et al. 2005; Takizawa et al. 2003). In the remaining five clusters, neither radio lobes nor luminous radio halos has been found in the central region in previous works, suggesting that they have not experienced strong AGN outbursts during past few tens of Myr, if the life time of such radio sources can be estimated by $t_{\text{sync}} = \frac{9m_e^3 c^5}{4e^4 B^2 \gamma_e}$ and $\bar{B} \sim 10 \mu\text{G}$ (Takahashi & Yamashita 2003; Donahue et al. 2005). As a unique case in our sample, A2556 harbors an off-center extended radio source at about $40''$ northeast of the center, which is often

¹<http://archive.stsci.edu/dss/>

²<http://www.ipac.caltech.edu/2mass/>

speculated to be the relic of a merger-driven shock (e.g., Govoni et al. 2004).

All the X-ray data analyzed in this work were acquired with the ACIS S3 CCD (Table 2), with the focal plane temperature set to be -120 °C. Using the CIAO v4.0 software and CALDB v3.5.0, we removed the bad pixels and columns, as well as events with *ASCA* grades 1, 5, and 7, and then executed the gain, CTI, and astrometry corrections. In order to identify possible strong background flares, lightcurves were extracted from regions sufficiently far away, i.e., $\geq 4'$ from the X-ray peaks. Time intervals during which the count rate exceeds the average quiescent value by 20 percent were excluded. The S1 chip data were used to crosscheck the results when it was available.

3. X-RAY IMAGING AND SPECTRAL ANALYSIS

3.1. X-Ray Images and Surface Brightness Profiles

Figure 1 shows the intensity contours of the X-ray emission in $0.3 - 10$ keV of our sample clusters, which overlay the corresponding optical DSS images. In all cases, the X-ray morphology appears to be smooth and symmetric on $> 100 h_{70}^{-1}$ kpc scales, showing no remarkable twists, fronts, or edges that indicate recent major mergers. On smaller scales, however, there exist substructures, such as X-ray cavities coinciding with the AGN lobes (Sun et al. 2003), stripes, filaments, and arc-like sharp fronts (Wise et al. 2004; Sanders et al. 2005).

For each cluster, we examine the vignetting-corrected surface brightness profile (SBP) extracted in $0.7 - 8.0$ keV, after filtering all the point sources that are detected above the 3σ level of the local background by using both the *celldetect* and *wavdetect* tools with their default settings (Fig. 2). By applying the χ^2 -test, we find that, except for the SBP of A2204, which can be well described with a single- β model $S(r) = S(0)(1 + (r/r_c)^2)^{-3\beta+1/2}$, all the obtained SBPs are consistent with the empirical two- β model $S(r) = S_1(0)(1 + (r/r_{c1})^2)^{-3\beta_1+1/2} + S_2(0)(1 + (r/r_{c2})^2)^{-3\beta_2+1/2}$ (e.g., Ikebe et al. 1996), because in the central $10 - 20 h_{70}^{-1}$ kpc (A1650, A2556, and A3112) or $20 - 40 h_{70}^{-1}$ kpc (A478, A1068, A1201, A2104, and A2244) there exists an emission excess beyond the β model that can best describe the SBPs of outer regions. Such an excess is often seen in clusters that host a central dominating galaxy, which is usually classified as a cD (Makishima et al. 2001).

3.2. Azimuthally-averaged Spectral Analysis

3.2.1. Background

In the spectral analysis that follows, we utilized the *Chandra* blank-sky templates for the S3 CCD as the background. The templates were tailored to match the actual pointings, and the background spectra were extracted and processed identically to the source spectra (§3.2.2). After rescaling each background spectrum by normalizing its high energy end to the corresponding observed spectrum, we further enhance the accuracy of the background by adding an unabsorbed APEC model with fixed temperature (0.2 keV) and metal abundance ($1 Z_{\odot}$; Snowden et al. 1998) to account for variations in the Galactic X-ray background (GXB; Vikhlinin et al. 2005). We note that the GXB component is significant only in A2204, where it has a flux of 2.0×10^{-14} erg s $^{-1}$ cm $^{-2}$ arcmin $^{-2}$ in 0.3 – 1.0 keV and is nearly uniform over the S3 chip. This was also reported by Sanders et al. (2009), who indicated that it is probably due to the excess Galactic foreground.

3.2.2. Models and Results

Here we calculate the azimuthally averaged temperature profiles, which will be used to create the reference temperature maps applied in wavelet detection (§3.3.2) and calculation of excess energies in the temperature substructures (§4). We divided the inner $400 h_{70}^{-1}$ kpc of each cluster into concentric annuli, masked all the detected point sources ($\simeq 15$ point sources per cluster), and extracted the spectrum from each annulus. The corresponding spectral redistribution matrix files (RMFs) and auxiliary response files (ARFs) were generated using the CIAO tool `mkwarf` and `mkacisrmf`. The spectra were grouped with > 20 counts per bin to allow the use of χ^2 statistics. We used XSPEC 12.4.0 package to fit the spectra, by modeling the gas emission with an absorbed APEC component and employing the PROJCT model to correct the projection effect. The absorption column density N_{H} was fixed to the Galactic value (Dickey & Lockman 1990) in all cases, except for A478, for which N_{H} was set to be about twice the Galactic value (Sanderson et al. 2005; Table 3); since the absorption excess in A478 exhibits a spatial extension beyond the cluster’s core region, Pointecouteau et al. (2004) argued that it is likely to be associated with a local absorption substructure in our Galaxy. In order to calculate the error ranges of the model parameters, we executed the XSPEC command `steppar` and carried out multiple iterations at every step, to ensure that the actual minimum χ^2 is found. The best-fit gas temperature and abundance profiles are illustrated in Figure 3, in which multiple sets of annuli are used for each cluster to crosscheck the results. We note that the inclusion of an additional gas component could only slightly

improve the fits for the central regions of A478, A1650, A2204, A2244, and A3112, which is insignificant as indicated by the F -test.

A significant temperature decline by a factor of > 2 is observed in the central regions of A478, A1068, A2204, A2556, and A3112, four of which (except A2556) possess radio halos and/or lobes in the center (§2). In the remaining four clusters without apparent radio emission, the inward temperature drop is somewhat ambiguous, as the difference between the core temperature and mean cluster temperature, which refer to the temperatures measured in the central $100 h_{70}^{-1}$ kpc ($\sim 0.1r_{500}$) and $100 - 400 h_{70}^{-1}$ kpc regions (Fig. 3), respectively, is found within 3σ error ranges. If we apply the classification criteria of Sanderson et al. (2006), the latter four clusters are non-cooling-core clusters, whose central regions have not yet fully condensed. These results reflect the trend for the cooling core clusters to host central radio sources (Burns 1990). As shown in Figure 3, we also adopt Eqs.(4) – (6) of Vikhlinin et al. (2006) to describe the obtained radial temperature profiles in a smooth form, which will be used in §3.3.2 to calculate the reference temperature maps in order to examine the significances of detected temperature substructures, and in §4 to calculate the excess energies in these substructures.

In A478, A1068, A1650, A2204, A2556, and A3112, the abundance increases inwards significantly (68% confidence level) from $\approx 0.2 Z_{\odot}$ in the outermost annuli to $> 0.6 Z_{\odot}$ in the innermost regions ($\lesssim 30 h_{70}^{-1}$ kpc). Emission measure-weighted gas temperature and abundance of each cluster are also calculated (Table 3), which are in good agreement with previous results obtained with *Chandra* and *XMM-Newton* (Sun et al. 2003; Takahashi & Yamashita 2003; Takizawa et al. 2003; Pointecouteau et al. 2004; Wise et al. 2004; Donahue et al. 2005; Sanders et al. 2005; Sanderson et al. 2005).

3.3. Two-Dimensional Analysis

3.3.1. Projected Temperature Maps

Following the methods of, e.g., O’Sullivan et al. (2005), Maughan et al. (2006), and Kanov et al. (2006), we define a set of knots \mathbf{r}_i (> 5000 knots per cluster) in the central $300 h_{70}^{-1}$ kpc region, which are randomly distributed with a separation of $\Delta_{ij} < 5''$ between any two adjacent knots i and j . To each knot we assign an adaptively sized circular cell, which is centered on the knot and contains more than 800 counts in $0.7 - 8$ keV after the background is subtracted. The typical cell radius ranges from $\lesssim 5''$ at the center to about $10''$ at $r \geq 150 h_{70}^{-1}$ kpc, which is always larger than the associated Δ_{ij} . We calculate the projected temperature of each cell $T_c(\mathbf{r}_i)$, which is assigned to the corresponding knot,

by fitting the spectrum extracted from the cell with an absorbed APEC model, using the absorption column given in Table 3; adding another thermal component can neither improve the fit significantly, nor make the parameters constrained more tightly. In the fittings, the source spectrum is grouped to have > 20 photons in each energy bin. In addition to the standard χ^2 statistics, we also have applied the maximum likelihood statistics, and find that the best-fit parameters obtained with the two statistics agree nicely with each other within the 1σ error ranges. The calculated 1σ errors of gas temperature are typically $< 10\%$ in the central $100 h_{70}^{-1}$ kpc, which increase progressively to $\lesssim 15\%$ (A478, A1650, A2244, and A3112) or $\lesssim 20\%$ (the remaining five clusters) in $100 - 300 h_{70}^{-1}$ kpc.

For any given position \mathbf{r} , we define a scale $s(\mathbf{r})$, so that there are at least 800 counts contained in a circular region centered at \mathbf{r} , whose radius is $s(\mathbf{r})$. We calculate the projected temperature at \mathbf{r} by integrating over all the knots \mathbf{r}_i located in the circular region,

$$T(\mathbf{r}) = \sum_{\mathbf{r}_i} (G_{\mathbf{r}_i}(R_{\mathbf{r},\mathbf{r}_i})T_c(\mathbf{r}_i)) / \sum_{\mathbf{r}_i} G_{\mathbf{r}_i}(R_{\mathbf{r},\mathbf{r}_i}), \text{ when } R_{\mathbf{r},\mathbf{r}_i} < s(\mathbf{r}), \quad (1)$$

where $R_{\mathbf{r},\mathbf{r}_i}$ is the distance from \mathbf{r} to \mathbf{r}_i , and $G_{\mathbf{r}_i}$ is the Gaussian kernel whose scale parameter σ is fixed at $s(\mathbf{r}_i)$. Since $s(\mathbf{r})$ is essentially proportional to the square root of the local counts, the obtained temperature map $T(\mathbf{r})$ (Fig. 4) is less affected by the statistical uncertainties caused by surface brightness fluctuations. In addition, angular resolutions of $\sim 10''$ are guaranteed by the use of compact Gaussian kernel. Maps for the upper and lower limits of $T(\mathbf{r})$ are calculated in a similar way.

3.3.2. Temperature Substructures

Wavelet Transform

A visual inspection of the obtained temperature maps (Fig. 4) indicates that there exist significant substructures, which typically have linear sizes of $\sim 100 h_{70}^{-1}$ kpc, in all of the sample clusters. In order to describe these substructures in a quantitative way, we analyze the statistical properties of the temperature maps by applying the wavelet transform, a powerful tool in imaging process that identifies and disentangles small embedded features as a function of scales (e.g., Vikhlinin et al. 1997; Starck & Pierre 1998). In an analogue study, Bourdin & Mazzotta (2008) conducted the wavelet transform to achieve an optimized spatial binning of temperature maps. We employ a non-orthogonal version of discrete wavelet transform, the à Trous wavelet (Shensa 1992; Starck et al. 1995; Vikhlinin et al. 1998), which defines a straightforward decomposition rule. To be specific, at position $\mathbf{r} = (x, y)$ and scale level i ($i = 1, 2, \dots$), the à Trous wavelet $w_i(x, y)$ equals the signal difference between two

smoothed maps $c_{i-1}(x, y) - c_i(x, y)$, where $c_0(x, y)$ is the obtained temperature map $T(x, y)$, and $c_i(x, y)$ connects with $c_{i-1}(x, y)$ via $c_i(x, y) = \sum_{m,n} h(m, n)c_{i-1}(x + 2^{i-1}m, y + 2^{i-1}n)$, in which $h(m, n)$ is the convolution kernel, and (m, n) is its grid. Here $h(m, n)$ is chosen to be a compact Gaussian $h(m, n) = e^{-(m^2+n^2)/2/2\pi}$. Each temperature map is thus decomposed into a set of subimages $w_i(x, y)$ on nine scales (2^i pixels, $i = 1, 2, \dots, 9$), respectively.

Based on the obtained $w_i(x, y)$ maps, we calculate the significant wavelet coefficient $W_i(x, y)$ to detect the temperature substructures on different scales. For each cluster, we create a set of random knots \mathbf{r}_i as used in §3.3.1, and assign a randomized temperature $T'_c(\mathbf{r}_i)$ to each knot, which is constrained by the measured temperature profile $T(r)$ and its error ranges (Fig. 3). By applying Eq.(1) to the $T'_c(\mathbf{r}_i)$ map, we obtain a reference temperature map $T_{\text{ref}}(\mathbf{r})$, in which the effects of the radial temperature gradients and knot tessellation are both involved. A series of such reference temperature maps are created by repeating this random process, and each reference map is decomposed into subimages $w_{i,\text{ref}}(x, y)$ on nine scales by performing the same à Trouis wavelet transform as described above. On each scale i , we determine the significant coefficient as $W_i(x, y) \equiv w_i(x, y)$ when $w_i(x, y) \geq 3\sigma_{i,\text{ref}}$, and $W_i(x, y) \equiv 0$ when $w_i(x, y) < 3\sigma_{i,\text{ref}}$ (e.g., Slezak et al. 1994; Starck et al. 2003), where $\sigma_{i,\text{ref}}$ is the standard deviation of the simulated $w_{i,\text{ref}}(x, y)$ maps so that $3\sigma_{i,\text{ref}}$ is equivalent to a confidence interval of 1.3×10^{-3} for Gaussian noise. A similar method was used to determine the actual significances of diffuse sources on *ROSAT* images (e.g., Rosati et al. 1995; Grebenev et al. 1995; Damiani et al. 1997).

Since the à Trouis transform is essentially a non-orthogonal algorithm, the obtained coefficient $w_i(x, y)$, and thus $W_i(x, y)$, may be systematically biased from the exact solution (Starck & Pierre 1998). This bias can be corrected by using an iterative method (Van Cittert 1931; Biviano et al. 1996; Starck et al. 2003; Bourdin et al. 2004), the iteration routine of which is defined as

$$W_i^n(x, y) = \begin{cases} W_i^0(x, y) + W_i^{n-1}(x, y) - PW_i^{n-1}(x, y) & W_i^0(x, y) \neq 0, \\ W_i^{n-1}(x, y) & W_i^0(x, y) = 0, \end{cases} \quad (2)$$

where $W_i^n(x, y)$ is the corrected detection on scale i after n iteration(s) ($W_i^0(x, y) \equiv W_i(x, y)$ is the initial run), and P is a non-linear synthesized operator of inverse wavelet transform, wavelet transform, and filtering operation using $3\sigma_{i,\text{ref}}$ as the threshold. Typically the calculation converges within five iterations, which yields a corrected $W_i(x, y)$ map as the unbiased reconstruction of the temperature substructures on scale i (Fig. 4). We define the wavelet spectrum as $\langle |W_i(x, y)|^2 \rangle$ (Torrence & Compo 1998), and plot it in Figure 5 as a function of scale for each cluster.

As a crosscheck, we also employ the two-dimensional B-spline function (e.g., Bourdin & Mazzotta 2008) as the scaling function $\phi(x, y)$ to perform a compact à Trouis trans-

form in the Fourier domain (u, v) , so that the Fourier transform of the wavelet coefficient $w_i(x, y)$ is directly calculated as $\hat{w}_i(u, v) = (1 - \hat{h}(2^{i-1}u, 2^{i-1}v))\hat{c}_{i-1}(u, v)$, where the filter $\hat{h}(u, v) = \hat{\phi}(2u, 2v)/\hat{\phi}(u, v)$ when $|u|, |v| \leq 1/2$ (in this paper the Fourier transform of any function f is written as \hat{f}). By carrying out the inverse Fourier transform to $\hat{w}_i(u, v)$, $w_i(x, y)$ maps are obtained, and then used to calculate the corrected $W_i(x, y)$ maps following the procedure described above. The corresponding wavelet spectra are illustrated in Figure 5 for comparison, which agree nicely with those obtained with the Gaussian wavelet. We find that the most popular scales of the projected temperature substructures are in the range of about $50 - 200 h_{70}^{-1}$ kpc, and about 70% of these substructures are located at $100 - 200 h_{70}^{-1}$ kpc from the cluster center, exhibiting irregular shapes and spatial distributions (Fig. 4).

Power Spectrum

As a straightforward approach, we have also studied the power spectra of the two-dimensional gas temperature distributions. Adopting the method of Schuecker et al. (2004), we determine the flat fields $\bar{T}(\mathbf{r})$ by applying a low-pass wavelet filter with a scale of 2^8 pixels on the original temperature maps, and calculate the normalized temperature fluctuation distributions as $\delta T(\mathbf{r}) = T(\mathbf{r})/\bar{T}(\mathbf{r}) - 1$. By carrying out the Fourier transform of $\delta T(\mathbf{r})$

$$\delta(\mathbf{k}) = \frac{1}{S} \int_S \delta T(\mathbf{r}) e^{i\mathbf{r}\cdot\mathbf{k}} d\mathbf{r}, \quad (3)$$

where S is the projected area, we obtain the power spectrum $P(k)$,

$$P(k) = \langle |\delta(\mathbf{k})|^2 \rangle. \quad (4)$$

Following the method of Schuecker et al. (2004), we carry out Monte-Carlo simulations for each cluster to estimate the temperature fluctuation at any given knot \mathbf{r}_i based on the temperature error range measured at the same knot (§3.3.1). After a randomized value $T_{\text{err}}(\mathbf{r}_i)$ is assigned to each knot, a random temperature error map $T_{\text{err}}(\mathbf{r})$ is created by applying Eq.(1) to the $T_{\text{err}}(\mathbf{r}_i)$ map, in which the uncertainties introduced by data statistics, spectral model fitting, and cell tessellation are all involved. Then, by combining $T(\mathbf{r})$ and $T_{\text{err}}(\mathbf{r})$ maps we create a random temperature map $T_{\text{ran}}(\mathbf{r})$. The 1σ error bars shown in Figure 6 are calculated from the variances of power spectra obtained from ten such $T_{\text{ran}}(\mathbf{r})$ maps for each cluster. In general, the power spectra $P(k)$ show a significant peak in $50 - 200 h_{70}^{-1}$ kpc, and drop quickly beyond $200 - 250 h_{70}^{-1}$ kpc. This strongly supports our conclusion derived with the wavelet analysis (Fig. 5).

4. DISCUSSION

We present robust evidence for the prevailing existence of hot gas clumps, whose characteristic scales are $\sim 100 h_{70}^{-1}$ kpc, in the central regions of a sample of nine intermediate-redshift galaxy clusters. These substructures are not caused by uncertainties in background subtraction, response calibration, and spectral model fittings, nor are they related to background flares, the effects of which have been largely corrected and/or fixed. The possibility of the temperature substructures arising from the non-thermal emission of low-mass X-ray binaries (LMXBs) can also be eliminated, since the ICM is only sparsely filled with galaxies. Our results confirm the previous findings in the Coma Cluster (Schuecker et al. 2004) and the Virgo Cluster (Shibata et al. 2001).

We estimate the excess thermal energy E_{excess} in each high temperature substructure (Table 4), where the gas temperature is typically higher than environment by $\Delta T_X \approx 2 - 3$ keV (Fig. 4), by defining the thermal energy as the product of gas pressure P and volume V , and assuming a spherical or elliptical geometry for the volume of the hot gas clump. We obtain $E_{\text{excess}} = \delta P \times V = \Delta T_X n_e V \sim 10^{58-60}$ erg for each clump, where n_e is the electron density determined in the deprojected spectral analysis (§3.2.2). To account for azimuthal variations in the electron density, we include a 10% systematic error (Sanders et al. 2004) in the calculations. As the projection effect is not corrected for ΔT_X , the obtained excess energy may have been underestimated by a factor of about two. The origin of this energy excess is discussed as follows.

4.1. Inhomogeneous Cooling, Conduction, and Turbulence

The detected temperature substructures may have been formed due to the spatially inhomogeneous cooling in the ICM. Since for a unit volume, the radiative cooling rate is $R_{\text{rad}} = n_e^2 \Lambda_{\text{rad}}(T, Z)$, where Λ_{rad} is the cooling function calculated by including both continuum and line emissions, the radiative cooling time of the substructures can be estimated as

$$t_{\text{cool}} \simeq \frac{n_e k_B T_X}{n_e^2 \Lambda_{\text{rad}}}. \quad (5)$$

Typically, the calculated cooling time is $\sim 10^{9-10}$ yrs, and is thus nearly an order of magnitude longer than the characteristic time for thermal conduction alone to smear out the temperature substructures (Table 4), which is given by

$$t_{\text{cond}} \simeq \frac{\delta h}{q} \delta r = \frac{\frac{5}{2} n_e k_B \delta T_X}{f \kappa_{\text{cond}} \frac{dT_X}{dr}} \delta r, \quad (6)$$

where δh is the enthalpy excess per unit volume in the hot substructure, q is the conductive flux, δr is the characteristic scale length of the substructure, $f = 0.2$ is the factor to assess the suppression caused by magnetic fields (e.g., Narayan & Medvedev 2001), and κ_{cond} is the thermal conductivity of hydrogen plasma,

$$\kappa_{\text{cond}} \simeq 5.0 \times 10^{-7} T_X^{\frac{5}{2}} [\text{erg cm}^{-1} \text{ s}^{-1} \text{ K}^{-1}] \quad (7)$$

for Coulomb gas (Spitzer 1962). This indicates that, unless the conduction process is extremely hindered (i.e., when $f \ll 1$; Maron et al. 2004; Markevitch et al. 2003), the effect of the radiative cooling is less important in the formation and evolution of temperature substructures. Hence the possibility of the substructures being formed by inhomogeneous cooling can be excluded.

The destruction of a temperature substructure via conduction can be accelerated by turbulence (Dennis & Chandran 2005), whose effect can be evaluated by introducing a modified conductivity (Cho et al. 2003; Voigt & Fabian 2004)

$$\kappa'_{\text{cond}} = \alpha n_e k_B l \left(\frac{5k_B T}{3\mu m_p} \right)^{1/2}, \quad (8)$$

where α is the ratio of the turbulence velocity v_{turb} to the local adiabatic sound speed c_s ($\alpha = v_{\text{turb}}/c_s$), and l is the turbulence length scale. To calculate κ'_{cond} , the turbulence velocity v_{turb} can be estimated as follows. As there is evidence that heating continuously compensates a large fraction of radiative cooling since $z \sim 0.4$ (Bauer et al. 2005; McNamara & Nulsen 2007), we may assume an approximate energy balance between heating and cooling for the cluster (e.g., Kim & Narayan 2003; Zakamska & Narayan 2003; Dennis & Chandran 2005) as

$$R \simeq H + \Gamma + Q, \quad (9)$$

where R is the radiative loss, and H , Γ and Q are the heating rates of thermal conduction, viscous dissipation and turbulent diffusion, respectively. Since

$$H = \nabla \cdot (\kappa_{\text{cond}} f \nabla T), \quad (10)$$

$$\Gamma = \frac{c_{\text{diss}} \rho v_{\text{turb}}^3}{l}, \quad (11)$$

and

$$Q = \nabla \cdot (D \rho T \nabla s), \quad (12)$$

where ρ is the gas mass density, s is the specific entropy, $c_{\text{diss}} \approx 0.42$ is a dimensionless constant (Dennis & Chandran 2005 and references therein), and $D \approx 10^{29} \text{ cm s}^{-1}$ is the

diffusion coefficient (Rebusco et al. 2006). By subtracting Eqs.(10) – (12) into Eq.(9), we have

$$v_{\text{turb}} = \left\{ [n_e^2 \Lambda_{\text{rad}} - \left(\frac{d\Psi}{dr} + \frac{2\Psi}{r} \right) - D \left(\frac{d\Theta}{dr} + \frac{2\Theta}{r} \right)] \frac{l}{c_{\text{diss}} \rho} \right\}^{\frac{1}{3}}, \quad (13)$$

if we define $\Psi = f \kappa_{\text{cond}} \frac{dT}{dr}$ and $\Theta = \rho T \frac{ds}{dr}$ (Dennis & Chandran 2005). Using the observed deprojected gas density and temperature profiles (Fig. 3), we calculate v_{turb} and show the results as a function of turbulence scale l in Figure 7. If we follow Schuecker et al. (2004) to adopt the lengths indicated by the turnover points on the wavelet spectra (Fig. 5) as the turbulence scale, we find that v_{turb} commonly ranges from 200 to 400 km s⁻¹, or $\alpha \sim 0.2-0.4$, for our sample. By using Eqs.(6) and (8), we find that the inclusion of turbulence reduces the characteristic time t_{cond} to the modified characteristic time t'_{cond} by a factor of about 3 (Table 4), which sets an upper limit ($\sim 10^8$ yrs) on the duty cycles of the dominating heating sources.

4.2. AGN Feedback

The calculated E_{excess} (Table 4) suggests that the hot clumps may be dying or remnants of buoyant bubbles, into which the central AGN has injected energy via shocks and turbulences (e.g., McNamara & Nulsen 2007). Such AGN-induced hot gas clumps are predicted in numerical simulations (e.g., Quilis et al. 2001; Dalla Vecchia et al. 2004; Vernaleo & Reynolds 2006) and theoretical calculations (e.g., Pizzolato & Soker 2006), whose scales are expected to be about 100 kpc by the end of the buoyancy process. By examining the temperature maps (Fig. 4), we note that some hot clumps appear in pairs on both sides of the central galaxies (#1 and #2 in A1201; #1 and #2 in A2204; #1 and #3 in A3112), which suggests possible AGN activity taking place at the cluster cores. However, can an AGN-heated temperature substructure survive conduction and turbulence destructions? To answer this question, we estimate the characteristic rising time of a bubble as $t_{\text{buoy}} = r_b / v_{\text{buoy}}$, where r_b is the travel distance measured from the cluster center to the location of a hot clump, and v_{buoy} is the travel velocity. In terms of the Keplerian velocity $v_K(r_b)$, a large bubble is expected to travel through the ambient gas at

$$v_{\text{buoy}}(r_b) \simeq \sqrt{\frac{8R_b}{3Cr_b}} v_K(r_b), \quad (14)$$

where $C \simeq 0.75$ is the drag coefficient and R_b is the bubble radius in kpc (Churazov et al. 2001). This yields t_{buoy} smaller or very close to t'_{cond} for $\approx 95\%$ of the substructures (Table 4), indicating that such substructures can survive in most cases. Even for the clumps with $t_{\text{buoy}} > t'_{\text{cond}}$, the AGN heating scenario may still stand, if the distance traveled by the bubble

is shorter (e.g., Gardini 2007). It should be noted that no hot gas clump is found associated with any known radio source in all sample clusters. This, however, does not contradict with the AGN heating scenario, because the lack of radio sources can be explained by the fact that the relativistic electrons may have lost most of their energy when the bubbles arose, as inferred by $t_{\text{sync}} \lesssim t_{\text{buoy}}$ ($t_{\text{sync}} \sim 10^{7-8}$ yrs; §2).

4.3. Other Possible Mechanisms

Numerical and theoretical works show that shocks caused by supersonic galaxy motion in the ICM can generate observable temperature substructures via gas compression and friction (e.g., El-Zant et al. 2004), and even the low-speed galaxy infalling may also be a heating source candidate due to the efficient energy conversion via the magnetohydrodynamic turbulence and magnetic reconnection (Makishima et al. 2001; reviewed by Markevitch & Vikhlinin 2007). The energy dissipation rate in the central region of a cluster is as large as 10^{44} erg s⁻¹ (Fujita et al. 2004), which assembles $\sim 10^{59}$ erg during the merger process and is thus sufficient to account for the excess energy in the observed temperature substructures. Nevertheless, no convincing evidence is given in numerical studies that the non-filamentary morphologies of the observed temperature substructures can appear commonly in merger process (e.g., Poole et al. 2006).

We also have estimated the contribution of supernova feedback to the ICM heating over the substructure lifetime (t'_{cond}) using the observed rate of type Ia supernovae (SNe Ia; Sharon et al. 2007), which implies that about $0.8 - 6.1 \times 10^7$ SN Ia explosions have occurred in the central $400 h_{70}^{-1}$ kpc region of each sample cluster. Since the averaged dynamic energy injection into the environment is 4×10^{50} erg per SN Ia event (Spitzer 1978), and $\sim 10\%$ of this energy is assumed to have been used to heat the gas (e.g., Thornton et al. 1998), the total SN Ia heating is found to be $< 3 \times 10^{57}$ erg per cluster per 10^8 yrs. The contribution of type II supernovae (SNe II) will not significantly increase the total supernova heating, since even in the IR-luminous cluster A1068, where the ratio of SN II rate to SN Ia rate is ≈ 3 (Wise et al. 2004), the SN II heating is still lower than 8×10^{57} erg. Therefore, we conclude that the supernova heating is insufficient to create the observed high temperature substructures.

High temperature substructures may also occur as a result of the inverse-Comptonization (IC) of the cosmic microwave background (CMB) photons that are scattered by the relativistic electrons in the ICM, since in a *Chandra* ACIS spectrum it is difficult to distinguish between such an IC component and a high temperature thermal component (Petrosian et al. 2008). If in the ICM 1% of the electrons are relativistic ($\gamma \sim 10^4$; Eilek 2003), we will

have an IC energy conversion rate of $b(\gamma) = \frac{4}{3} \frac{\sigma_T}{m_e c} \gamma^2 U_{\text{CMB}} \simeq 6 \times 10^{44} \text{ erg s}^{-1}$, where σ_T is the Thomson cross section and U_{CMB} is the CMB energy density at the location of the cluster (Sarazin 1999), which implies that the flux of the IC component is sufficiently high to bias the temperature measurements by about 1 – 3 keV. However, a tight correlation between the high temperature substructures and radio synchrotron sources is required in this scenario, which is actually not observed, possibly due to the lack of relativistic electrons. Therefore, the IC mechanism for the formation of the temperature substructures can be eliminated.

5. SUMMARY

We reveal the prevailing existence of temperature substructures on $\sim 100 h_{70}^{-1}$ kpc scales in the central regions of nine intermediate-redshift galaxy clusters. By comparing the characteristic destruction times of the temperature substructures with the gas cooling times and the rising times of AGN-induced bubbles, we conclude that the AGN outbursts may have played a crucial role in the forming of the observed temperature substructures. Our results agree with those found earlier in the Virgo and Coma Clusters (Shibata et al. 2001; Schuecker et al. 2004).

Acknowledgments

We thank Kazuo Makishima, Kazuhiro Nakazawa, Peter Schuecker, and Hervé Bourdin for their helpful suggestions and comments. This work was supported by the National Science Foundation of China (Grant No. 10673008 and 10878001), the Ministry of Science and Technology of China (Grant No. 2009CB824900/2009CB24904), and the Ministry of Education of China (the NCET Program).

REFERENCES

- Abell, G. O., Corwin, H. G., & Olowin, R. P. 1989, *ApJS*, 70, 1
- Arnaud, M., Pointecouteau, E., & Pratt, G. W. 2005, *A&A*, 441, 893
- Bauer, F. E., Fabian, A. C., Sanders, J. S., Allen, S. W., & Johnstone, R. M. 2005, *MNRAS*, 359, 1481
- Biviano, A., Durret, F., Gerbal, D., Le Fevre, O., Lobo, C., Mazure, A., & Slezak, E. 1996, *A&A*, 311, 95

- Blanton, E. L., Sarazin, C. L., & McNamara, B. R. 2003, *ApJ*, 585, 227
- Bourdin, H., Sauvageot, J.-L., Slezak, E., Bijaoui, A., & Teyssier, R. 2004, *A&A*, 414, 429
- Bourdin, H., & Mazzotta, P. 2008, *A&A*, 479, 307
- Bregman, J. N., & David, L. P. 1989, *ApJ*, 341, 49
- Burns, J. O. 1990, *AJ*, 99, 14
- Cho, J., Lazarian, A., Honein, A., Knaepen, B., Kassinos, S., & Moin, P. 2003, *ApJ*, 589, L77
- Churazov, E., Brüggén, M., Kaiser, C. R., Böhringer, H., & Forman, W. 2001, *ApJ*, 554, 261
- Croston, J. H., Hardcastle, M. J., & Birkinshaw, M. 2005, *MNRAS*, 357, 279
- Dalla Vecchia, C., Bower, R. G., Theuns, T., Balogh, M. L., Mazzotta, P., & Frenk, C. S. 2004, *MNRAS*, 355, 995
- Damiani, F., Maggio, A., Micela, G., & Sciortino, S. 1997, *ApJ*, 483, 350
- Dennis, T. J., & Chandran, B. D. G. 2005, *ApJ*, 622, 205
- Dickey, J. M., & Lockman, F. J. 1990, *ARA&A*, 28, 215
- Donahue, M., Voit, G. M., O’Dea, C. P., Baum, S. A., & Sparks, W. B. 2005, *ApJ*, 630, L13
- Edge, A. C., & Stewart, G. C. 1991, *MNRAS*, 252, 414
- Eilek, J. A. 2003, *Phys. Plasmas*, 10, 1539
- Eke, V. R., Cole, S., Frenk, C. S., & Patrick H., J. 1998, *MNRAS*, 298, 1145
- El-Zant, A. A., Kim, W.-T., & Kamionkowski, M. 2004, *MNRAS*, 354, 169
- Evrard, A. E., & Henry, J. P. 1991, *ApJ*, 383, 95
- Evrard, A. E., Metzler, C. A., & Navarro, J. F. 1996, *ApJ*, 469, 494
- Fabian, A. C. 1994a, *ARA&A*, 32, 277
- Fabian, A. C., Crawford, C. S., Edge, A. C., & Mushotzky, R. F. 1994b, *MNRAS*, 267, 779
- Fabian, A. C., Sanders, J. S., Ettori, S., Taylor, G. B., Allen, S. W., Crawford, C. S., Iwasawa, K., Johnstone, R. M., & Ogle, P. M. 2000, *MNRAS*, 318, L65
- Fabian, A. C., Sanders, J. S., Taylor, G. B., & Allen, S. W. 2005, *MNRAS*, 360, L20
- Frenk, C. S., Baugh, C. M., & Cole, S. M. 1996, *IAU Symposia* 171, 247
- Fujita, Y., Matsumoto, T., & Wada, K. 2004, *ApJ*, 612, L9
- Gardini, A. 2007, *A&A*, 464, 143

- Govoni, F., Markevitch, M., Vikhlinin, A., VanSpeybroeck, L., Feretti, L., & Giovannini, G. 2004, *ApJ*, 605, 695
- Grebenev, S. A., Forman, W., Jones, C., & Murray, S. 1995, *ApJ*, 445, 607
- Grevesse, N., & Sauval, A. J. 1998, *Space Sci. Rev.*, 85, 161
- Horner, D. J., Mushotzky, R. F., & Scharf, C. A. 1999, *ApJ*, 520, 78
- Ikebe, Y., Ezawa, H., Fukazawa, Y., Hirayama, M., Ishisaki, Y., Kikuchi, K., Kubo, H., Makishima, K., Matsushita, K., Ohashi, T., Takahashi, T., & Tamura, T. 1996, *Nature*, 379, 427
- Jetha, N. N., Ponman, T. J., Hardcastle, M. J., & Croston, J. H. 2007, *MNRAS*, 376, 193
- Kaiser, N. 1991, *ApJ*, 383, 104
- Kanov, K. N., Sarazin, C. L., & Hicks, A. K. 2006, *ApJ*, 653, 184
- Kauffmann, G., White, S. D. M., & Guiderdoni, B. 1993, *MNRAS*, 264, 201
- Kim, W.-T., & Narayan, R. 2003, *ApJ*, 596, 889
- Kotov, O., & Vikhlinin, A. 2006, *ApJ*, 641, 752
- Makishima, K., Ezawa, H., Fukuzawa, Y., Honda, H., Ikebe, Y., Kamae, T., Kikuchi, K., Matsushita, K., Nakazawa, K., Ohashi, T., Takahashi, T., Tamura, T., & Xu, H. 2001, *PASJ*, 53, 401
- Markevitch, M., & Vikhlinin, A. 2001, *ApJ*, 563, 95
- Markevitch, M., Mazzotta, P., Vikhlinin, A., Burke, D., Butt, Y., David, L., Donnelly, H., Forman, W. R., Harris, D., Kim, D.-W., Virani, S., & Vrtilik, J. 2003, *ApJ*, 586, L19
- Markevitch, M., & Vikhlinin, A. 2007, *Phys. Rep.*, 443, 1
- Maron, J., Chandran, B. D., & Blackman, E. 2004, *Phys. Rev. Lett.*, 92, 045001
- Maughan, B. J., Ellis, S. C., Jones, L. R., Mason, K. O., Córdova, F. A., & Priedhorsky, W. 2006, *ApJ*, 640, 219
- McNamara, B. R., Wise, M. W., & Murray, S. S. 2004, *ApJ*, 601, 173
- McNamara, B. R., & Nulsen, P. E. J. 2007, *ARA&A*, 45, 117
- Mohr, J. J., & Evrard, A. E. 1997, *ApJ*, 491, 38
- Mushotzky, R. F. 1984, *Phys. Scr.*, 7, 157
- Narayan, R., & Medvedev, M. V. 2001, *ApJ*, 562, L129
- Navarro, J. F., Frenk, C. S., & White, S. D. M. 1995, *MNRAS*, 275, 720

- Nulsen, P. E. J., David, L. P., McNamara, B. R., Jones, C., Forman, W. R., & Wise, M. 2002, *ApJ*, 568, 163
- O’Sullivan, E., Vrtilik, J. M., Kempner, J. C., David, L. P., & Houck, J. C. 2005, *MNRAS*, 357, 1134
- Peterson, J. R., Kahn, S. M., Paerels, F. B. S., Kaastra, J. S., Tamura, T., Bleeker, J. A. M., Ferrigno, C., & Jernigan, J. G. 2003, *ApJ*, 590, 207
- Petrosian, V., Bykov, A., & Rephaeli, Y. 2008, *Space Sci. Rev.*, 134, 191
- Pizzolato, F., & Soker, N. 2006, *MNRAS*, 371, 1835
- Pointecouteau, E., Arnaud, M., Kaastra, J., & de Plaa, J. 2004, *A&A*, 423, 33
- Ponman, T. J., Cannon, D. B., & Navarro, J. F. 1999, *Nature*, 397, 135
- Ponman, T. J., Sanderson, A. J. R., & Finoguenov, A. 2003, *MNRAS*, 343, 331
- Poole, G. B., Fardal, M. A., Babul, A., McCarthy, I. G., Quinn, T., & Wadsley, J. 2006, *MNRAS*, 373, 881
- Quilis, V., Bower, R. G., & Balogh, M. L. 2001, *MNRAS*, 328, 1091
- Rebusco, P., Churazov, E., Böhringer, H., & Forman, W. 2006, *MNRAS*, 372, 1840
- Rood, H. J., & Sastry, G. N. 1971, *PASP*, 83, 313
- Rosati, P., della Ceca, R., Burg, R., Norman, C., & Giacconi, R. 1995, *ApJ*, 445, L11
- Sanders, J. S., Fabian, A. C., Allen, S. W., & Schmidt, R. W. 2004, *MNRAS*, 349, 952
- Sanders, J. S., Fabian, A. C., & Taylor, G. B. 2005, *MNRAS*, 356, 1022
- Sanders, J. S., Fabian, A. C., & Taylor, G. B. 2009, *MNRAS*, 393, 71
- Sanderson, A. J. R., Finoguenov, A., & Mohr, J. J. 2005, *ApJ*, 630, 191
- Sanderson, A. J. R., Ponman, T. J., & O’Sullivan, E. 2006, *MNRAS*, 372, 1496
- Sarazin, C. L. 1999, *ApJ*, 520, 529
- Schombert, J. M., West, M. J., Zucker, J. R., & Struble, M. F. 1989, *AJ*, 98, 1999
- Schuecker, P., Finoguenov, A., Miniati, F., Böhringer, H., & Briel, U. G. 2004, *A&A*, 426, 387
- Sharon, K., Gal-Yam, A., Maoz, D., Filippenko, A. V., & Guhathakurta, P. 2007, *ApJ*, 60, 1165
- Shensa, M. J. 1992, *IEEE Trans. Sig. Proc.*, 40, 2464
- Shibata, R., Matsushita, K., Yamasaki, N. Y., Ohashi, T., Ishida, M., Kikuchi, K., Böhringer, H., & Matsumoto, H. 2001, *ApJ*, 549, 228

- Slezak, E., Durret, F., & Gerbal, D. 1994, *AJ*, 108, 1996
- Snowden, S. L., Egger, R., Finkbeiner, D., Freyberg, M. J., & Plucinsky, P. P. 1998, *ApJ*, 493, 715
- Spitzer, L. 1962, *Physics of Fully Ionized Gases* (New York: Interscience)
- Spitzer, L. 1978, *Physical Processes in the Interstellar Medium* (New York: John Wiley & Sons)
- Starck, J.-L., Murtagh, F., & Bijaoui, A. 1995, *ADASS Conf. Proc. ASP Conf. Series*, 77, 279
- Starck, J.-L., & Pierre, M. 1998, *A&AS*, 128, 397
- Starck, J. L., Donoho, D. L., & Candès, E. J. 2003, *A&A*, 398, 785
- Struble, M. F., & Rood, H. J. 1987, *ApJS*, 63, 555
- Sun, M., Jones, C., Murray, S. S., Allen, S. W., Fabian, A. C., & Edge, A. C. 2003, *ApJ*, 587, 619
- Takahashi, S., & Yamashita, K. 2003, *PASJ*, 55, 1105
- Takizawa, M., Sarazin, C. L., Blanton, E. L., & Taylor, G. B. 2003, *ApJ*, 595, 142
- Thornton, K., Gaudlitz, M., Janka, H.-Th., & Steinmetz, M. 1998, *ApJ*, 500, 95
- Torrence, C., & Compo, G. P. 1998, *Bull. Amer. Met. Soc.*, 79, 61
- Tozzi, P., & Norman, C. 2001, *ApJ*, 546, 63
- Van Cittert, P. H. 1931, *Z. Phys.*, 69, 298
- Vernaleo, J. C., & Reynolds, C. S., 2006, *ApJ*, 645, 83
- Vikhlinin, A., Forman, W., & Jones, C. 1997, *ApJ*, 474, L7
- Vikhlinin, A., McNamara, B. R., Forman, W., Jones, C., Quintana, H., & Hornstrup, A. 1998, *ApJ*, 502, 558
- Vikhlinin, A., Markevitch, M., & Murray, S. S. 2001, *ApJ*, 551, 160
- Vikhlinin, A., Markevitch, M., Murray, S. S., Jones, C., Forman, W., & Van Speybroeck, L. 2005, *ApJ*, 628, 665
- Vikhlinin, A., Kravtsov, A., Forman, W., Jones, C., Markevitch, M., Murray, S. S., & Van Speybroeck, L. 2006, *ApJ*, 640, 691
- Voigt, L. M., & Fabian, A. C. 2004, *MNRAS*, 347, 1130
- Wise, M. W., McNamara, B. R., & Murray, S. S. 2004, *ApJ*, 601, 184
- Xu, H., Jin, G., & Wu, X.-P. 2001, *ApJ*, 553, 78

Zakamska, N. L., & Narayan, R. 2003, ApJ, 582, 162

Table 1. Galaxy Clusters in Our Sample

Name	cD Galaxy	Redshift	R ^a	RA ^b (h d s; J2000)	DEC ^b (d m s; J2000)	Notes ^c
A0478	2MASX J04132526+1027551	0.0881	2	04 13 20.7	+10 28 35	1,3
A1068	2MASX J10404446+3957117	0.1375	1	10 40 47.1	+39 57 19	2,3
A1201	–	0.1688	2	11 13 01.1	+13 25 40	
A1650	2MASX J12584149–0145410	0.0845	2	12 58 46.2	–01 45 11	
A2104	–	0.1554	2	15 40 06.8	–03 17 39	
A2204	–	0.1523	3	16 32 45.7	+05 34 43	2,3
A2244	FIRST J170242.5+340337	0.0968	2	17 02 44.0	+34 02 48	
A2556	–	0.0871	1	23 13 01.6	–21 37 59	4
A3112	ESO 248- G 006	0.0750	2	03 17 52.4	–44 14 35	3

^aAbell richness class (Abell et al. 1989).

^bPositions of the cluster optical centroids.

^cX-ray and radio substructures in the clusters, including 1 – X-ray cavities, 2 – cold fronts, 3 – central radio sources, and 4 – off-center radio source.

Table 2. Observation Log

Target	ObsID	ACIS CCD	Mode	Date dd mm yyyy	Raw/Clean Exposure (ks)
A0478	1669	235678	FAINT	27/01/2001	42.9/41.9
A1068	1652	236789	FAINT	04/02/2001	27.2/26.0
A1201	4216	35678	VFAINT	01/11/2003	40.2/25.4
A1650	4178	35678	VFAINT	03/08/2003	27.6/26.0
A2104	895	235678	FAINT	25/05/2000	49.8/48.1
A2204	499	235678	FAINT	29/07/2000	10.2/9.3
A2244	4179	35678	VFAINT	10/10/2003	57.7/56.0
A2556	2226	35678	VFAINT	05/10/2001	20.2/19.8
A3112	2516	35678	VFAINT	15/09/2001	17.2/15.1

Table 3. Global Properties of the Halo Gas^a

Name	Aperture (h_{70}^{-1} kpc)	kT (keV)	Abundance (Z_{\odot})	N_{H}^{b} (10^{20} cm $^{-2}$)
A0478	405.4	$6.93^{+0.20}_{-0.26}$	$0.47^{+0.03}_{-0.03}$	$26.75^{+0.72}_{-0.51}$
A1068	418.7	$3.63^{+0.10}_{-0.10}$	$0.56^{+0.04}_{-0.04}$	1.40
A1201	425.5	$4.81^{+0.35}_{-0.44}$	$0.32^{+0.11}_{-0.09}$	1.61
A1650	390.5	$5.96^{+0.24}_{-0.25}$	$0.48^{+0.07}_{-0.08}$	1.56
A2104	397.6	$9.60^{+0.77}_{-0.76}$	$0.47^{+0.07}_{-0.08}$	8.69
A2204	391.0	$7.24^{+0.43}_{-0.53}$	$0.51^{+0.06}_{-0.07}$	5.67
A2244	396.9	$5.25^{+0.10}_{-0.08}$	$0.29^{+0.03}_{-0.03}$	2.14
A2556	401.3	$3.17^{+0.09}_{-0.10}$	$0.43^{+0.05}_{-0.04}$	2.05
A3112	385.5	$4.03^{+0.13}_{-0.12}$	$0.79^{+0.08}_{-0.07}$	2.61

^aAn absorbed APEC model is used to estimate the emission measure-weighted gas temperatures kT and abundances. The error bars are given at 90% confidence level.

^bColumn densities are fixed to the Galactic values (Dickey & Lockman 1990), except for A478, which shows an absorption larger than the Galactic value (15.1×10^{20} cm $^{-2}$).

Table 4. Characteristic Timescales for the Detected Temperature Substructures

No. ^a	r ^b (h_{70}^{-1} kpc)	n_e ^c (cm^{-3})	E_{excess} ^d (10^{58} erg)	t_{cool} ^e (10^8 yrs)	t_{cond} ^f (10^8 yrs)	t'_{cond} ^g (10^8 yrs)	t_{buoy} ^h (10^8 yrs)
A0478[1]	95	0.016	1.9 ± 0.8	16.4 ± 5.2	7.7 ± 2.0	1.9 ± 0.4	1.6
[2]	141	0.010	7.4 ± 2.2	23.8 ± 6.1	3.2 ± 0.8	1.7 ± 0.6	2.0
[3]	155	0.009	7.2 ± 3.7	30.0 ± 7.4	2.4 ± 0.4	1.7 ± 0.6	2.2
[4]	157	0.009	4.3 ± 2.5	33.6 ± 8.1	4.7 ± 0.8	2.3 ± 0.5	2.3
A1068[1]	184	0.004	11.0 ± 4.8	54.6 ± 13.8	16.7 ± 2.2	2.2 ± 0.8	2.7
[2]	237	0.002	14.6 ± 8.7	106.2 ± 19.8	8.7 ± 2.2	5.4 ± 1.5	3.2
[3]	244	0.002	32.2 ± 15.8	135.9 ± 30.4	10.3 ± 2.9	5.3 ± 1.6	3.3
A1201[1]	123	0.005	17.4 ± 10.8	69.1 ± 16.7	5.8 ± 1.2	4.2 ± 0.9	2.0
[2]	171	0.003	36.0 ± 20.7	87.6 ± 17.8	11.1 ± 2.1	5.9 ± 1.4	2.7
[3]	185	0.003	29.3 ± 16.7	118.4 ± 30.5	9.2 ± 1.7	4.7 ± 1.0	2.9
A1650[1]	72	0.013	4.6 ± 2.0	26.1 ± 12.0	3.2 ± 1.2	1.5 ± 0.8	2.4
[2]	108	0.007	12.2 ± 5.2	42.3 ± 12.9	6.3 ± 2.3	2.2 ± 0.5	2.9
[3]	113	0.007	4.6 ± 1.5	38.7 ± 12.2	4.7 ± 1.4	2.3 ± 0.5	3.0
[4]	171	0.005	12.6 ± 4.5	61.5 ± 13.6	2.8 ± 1.1	2.5 ± 1.1	3.6
A2104[1]	132	0.007	7.0 ± 5.6	53.7 ± 16.8	3.4 ± 0.7	2.7 ± 0.5	2.8
[2]	253	0.003	47.8 ± 26.5	87.7 ± 17.8	1.8 ± 0.5	0.4 ± 0.3	4.0
[3]	261	0.003	41.5 ± 23.9	122.8 ± 31.2	1.7 ± 0.5	0.2 ± 0.3	4.1
A2204[1]	94	0.017	65.8 ± 26.1	22.8 ± 6.5	1.5 ± 0.5	1.4 ± 0.5	1.4
[2]	117	0.013	54.0 ± 26.8	22.8 ± 6.8	3.5 ± 0.6	1.9 ± 0.5	1.6
[3]	172	0.009	145.7 ± 72.3	47.2 ± 11.7	6.0 ± 1.6	2.9 ± 1.0	2.0
[4]	220	0.006	104.4 ± 42.1	61.8 ± 13.9	2.8 ± 0.9	2.1 ± 0.8	2.4
A2244[1]	74	0.014	3.6 ± 1.0	22.7 ± 6.1	15.0 ± 0.9	2.5 ± 0.5	1.3
[2]	100	0.010	8.5 ± 3.2	29.8 ± 7.8	8.9 ± 0.7	2.5 ± 0.5	1.7
[3]	155	0.006	4.9 ± 2.1	42.0 ± 13.0	6.4 ± 0.8	2.5 ± 0.6	2.3
A2556[1]	108	0.005	13.6 ± 3.8	62.3 ± 12.8	13.9 ± 2.1	3.7 ± 0.8	1.8
[2]	141	0.004	13.0 ± 2.2	70.8 ± 12.0	10.7 ± 1.5	3.2 ± 0.7	2.3
[3]	144	0.004	7.0 ± 3.6	65.3 ± 15.4	16.0 ± 2.6	3.6 ± 0.9	2.3
A3112[1]	73	0.014	2.9 ± 1.3	20.2 ± 6.4	9.5 ± 1.1	1.9 ± 0.6	1.2
[2]	121	0.006	5.2 ± 2.2	45.1 ± 9.1	11.4 ± 1.5	2.9 ± 0.7	1.8
[3]	125	0.006	6.8 ± 3.6	41.9 ± 9.5	7.2 ± 1.2	2.2 ± 0.6	1.9
[4]	141	0.006	3.8 ± 2.2	39.6 ± 9.6	2.8 ± 0.8	2.1 ± 0.6	2.0

^aDetected temperature substructures. See Figure 4.

^bDistances between the geometric centers of the substructures and the cluster centers.

^cAveraged electron densities of the substructures.

^dExcess thermal energies contained in the substructures.

^eRadiative cooling times of the substructures.

^fDestruction times of the substructures due to thermal conduction (Eq.(6)).

^gModified destruction times of the substructures due to thermal conduction, viscous dissipation, and turbulent diffusion (Eq.(8)).

^hRising times of the temperature substructures if they are AGN-induced bubbles.

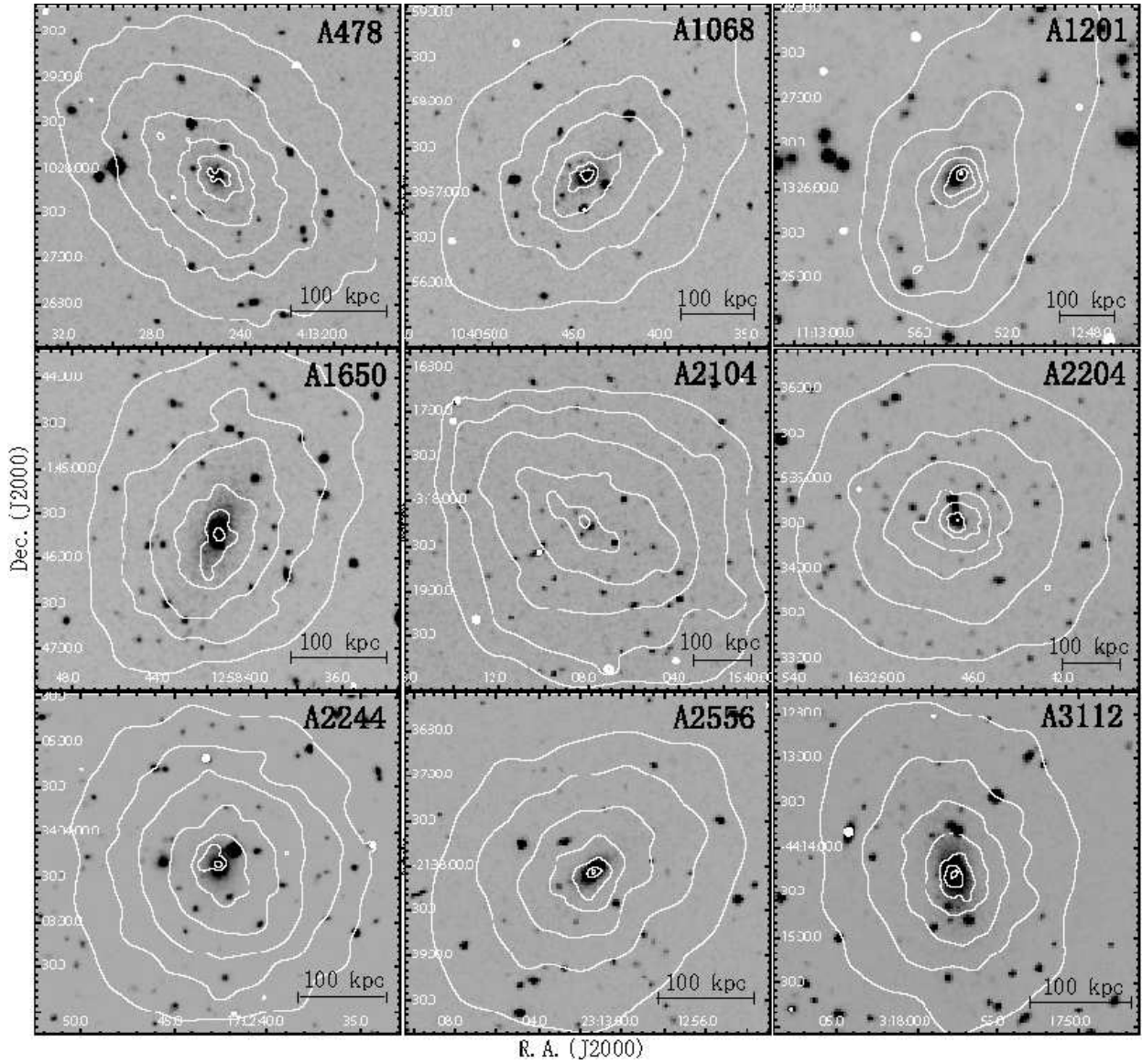


Fig. 1.— DSS optical images of the sample clusters, on which the 0.3 – 10.0 keV X-ray intensity contours are plotted. To calculate the X-ray contours we subtract the background, correct the exposure, and smooth the image with a minimum signal-to-noise (S/N) of 3 and a maximum S/N of 5 per smoothing beam.

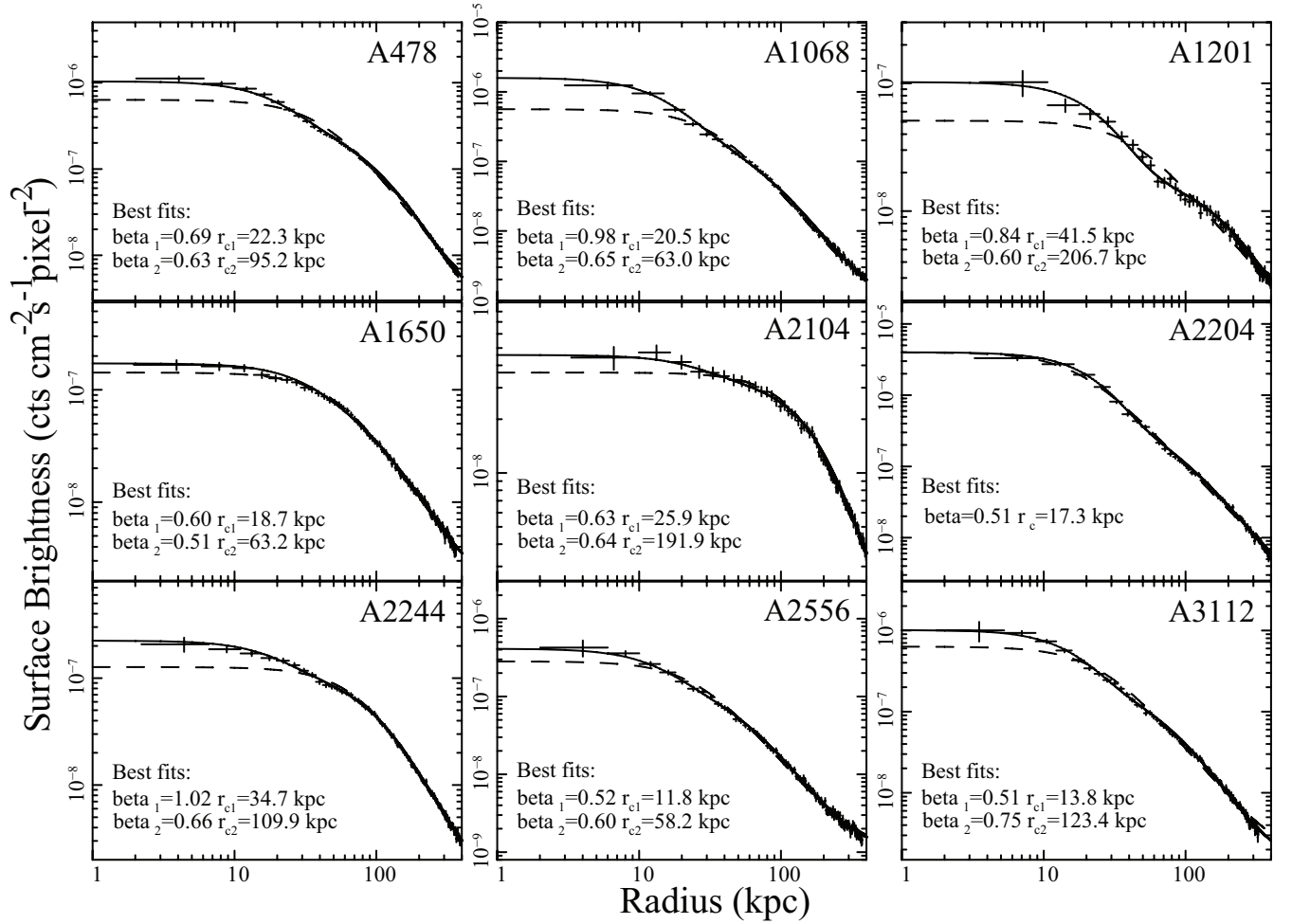


Fig. 2.— Radial surface brightness profiles extracted in 0.7 – 8.0 keV, which are corrected for both background and exposure. The best-fit two- β and β models are shown with solid and dash lines, respectively. For A2204 only the β model is plotted, which is sufficient to describe its SBP.

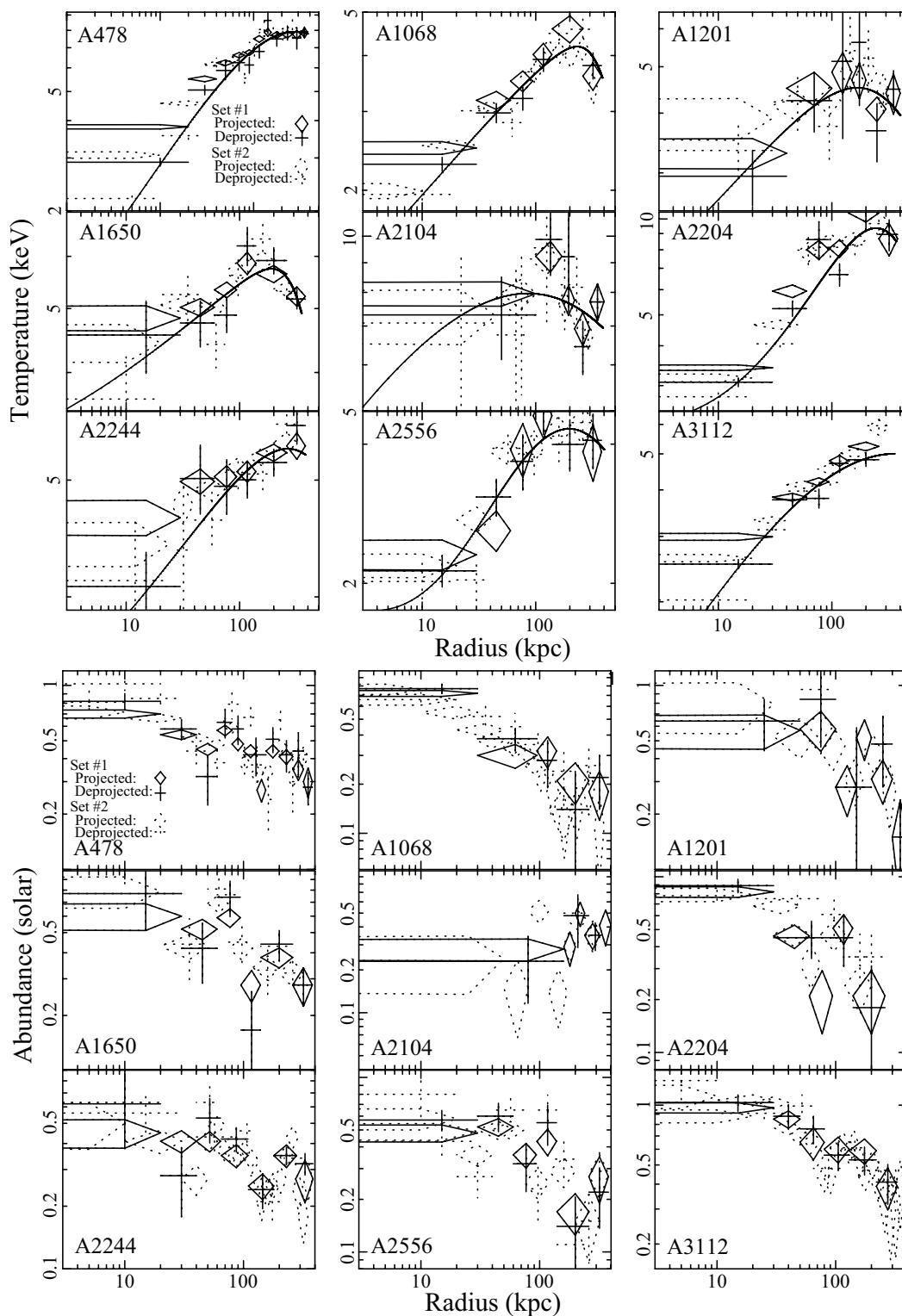


Fig. 3.— Projected and deprojected temperature (*upper panel*) and abundance profiles (*lower panel*) for two sets of annuli. Error bars are given at 90% and 68% confidence levels for temperature and abundance profiles, respectively.

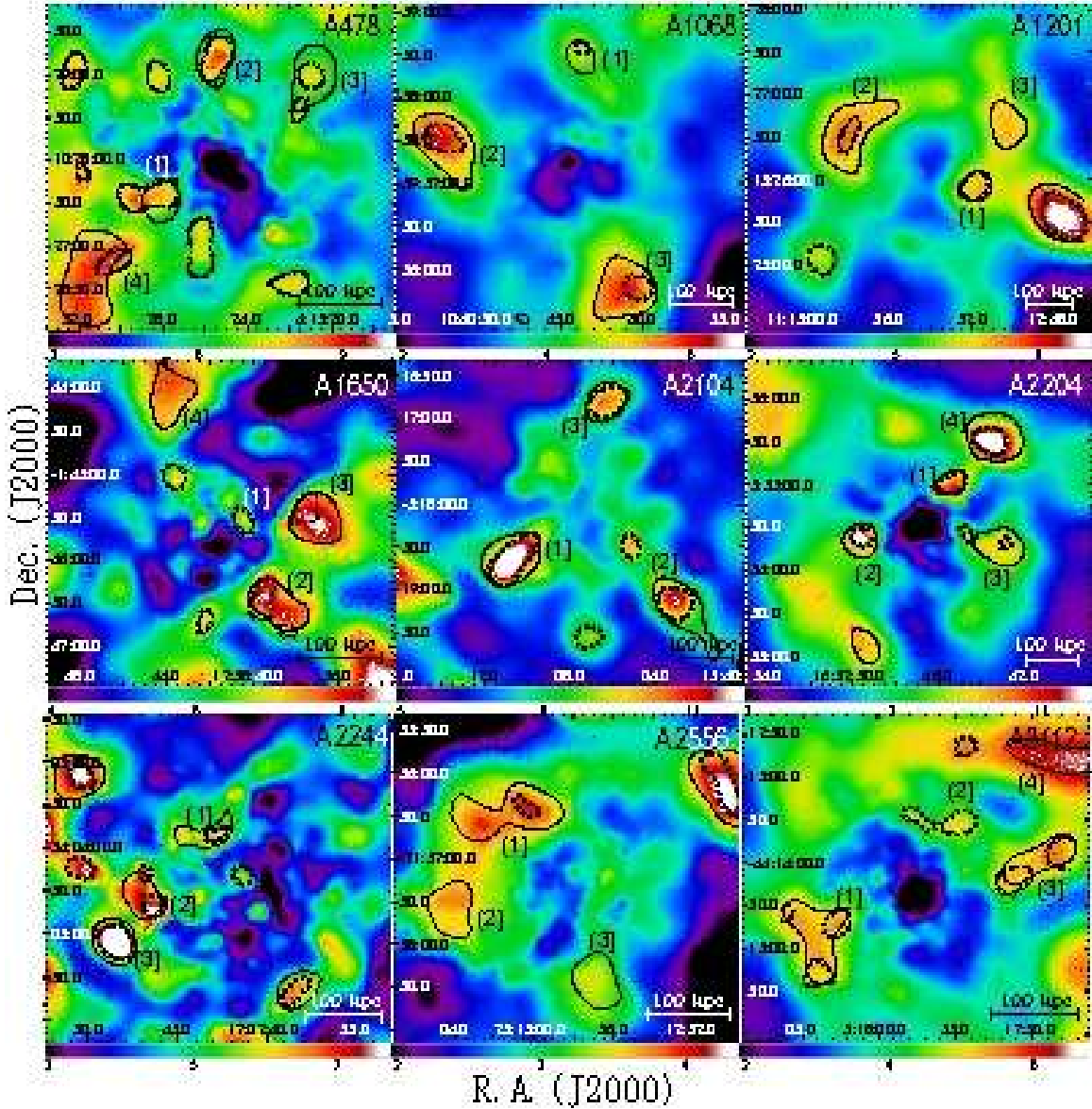


Fig. 4.— Projected temperature maps, on which the most significant substructures with the characteristic scales indicated by the wavelet spectra (Fig. 5), i.e., $i = 7$ ($100 - 200 h_{70}^{-1}$ kpc; solid line) and $i = 6$ ($50 - 100 h_{70}^{-1}$ kpc; dotted line) are marked (§3.3.2). The representative substructures are labeled with the same numbers as used in Table 4.

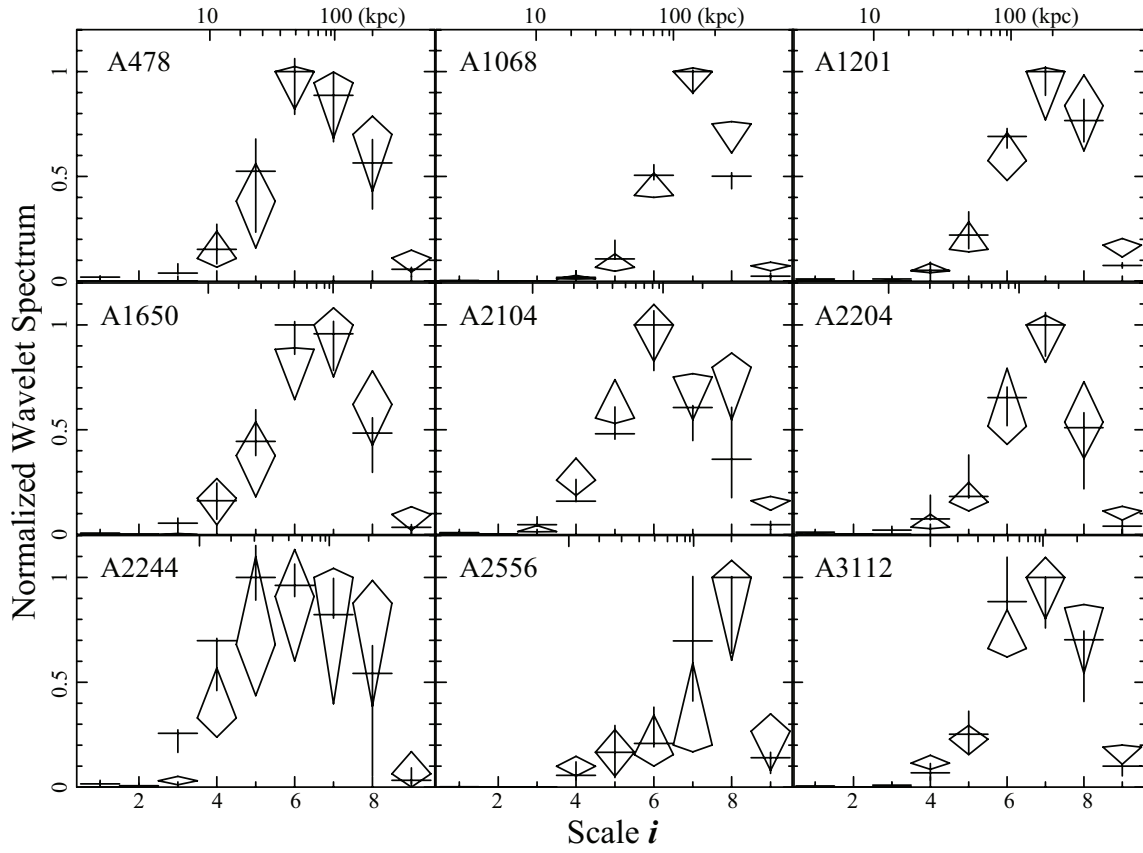


Fig. 5.— Wavelet spectra of the two-dimensional temperature distributions $T(\mathbf{r})$ derived with both the Gaussian wavelet (cross) and the B-spline wavelet (diamond). Error bars are given at 1σ confidence level (§3.3.2).

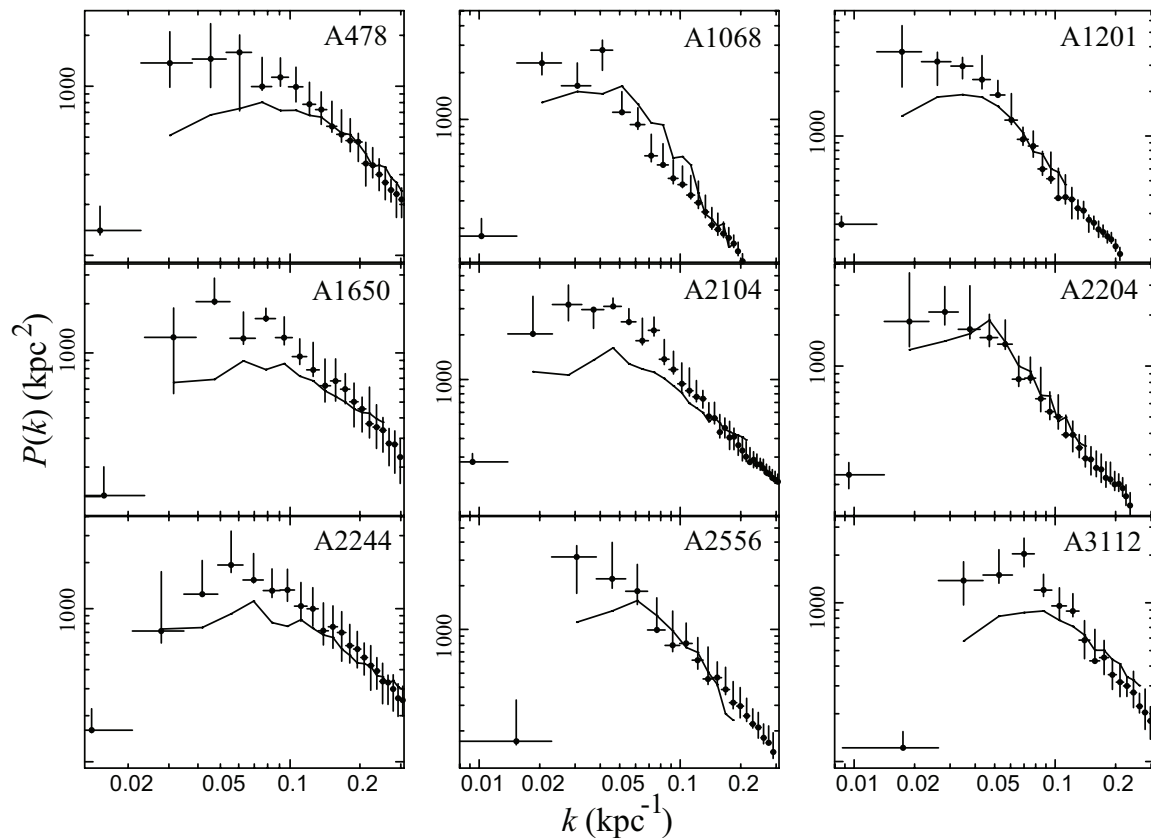


Fig. 6.— Power spectra of the two-dimensional temperature distributions $T(\mathbf{r})$ (cross) and simulated reference temperature maps $T_{\text{ref}}(\mathbf{r})$ (solid line). 1σ error bars are determined by applying the Monte-Carlo approach introduced in Schuecker et al. (2004).

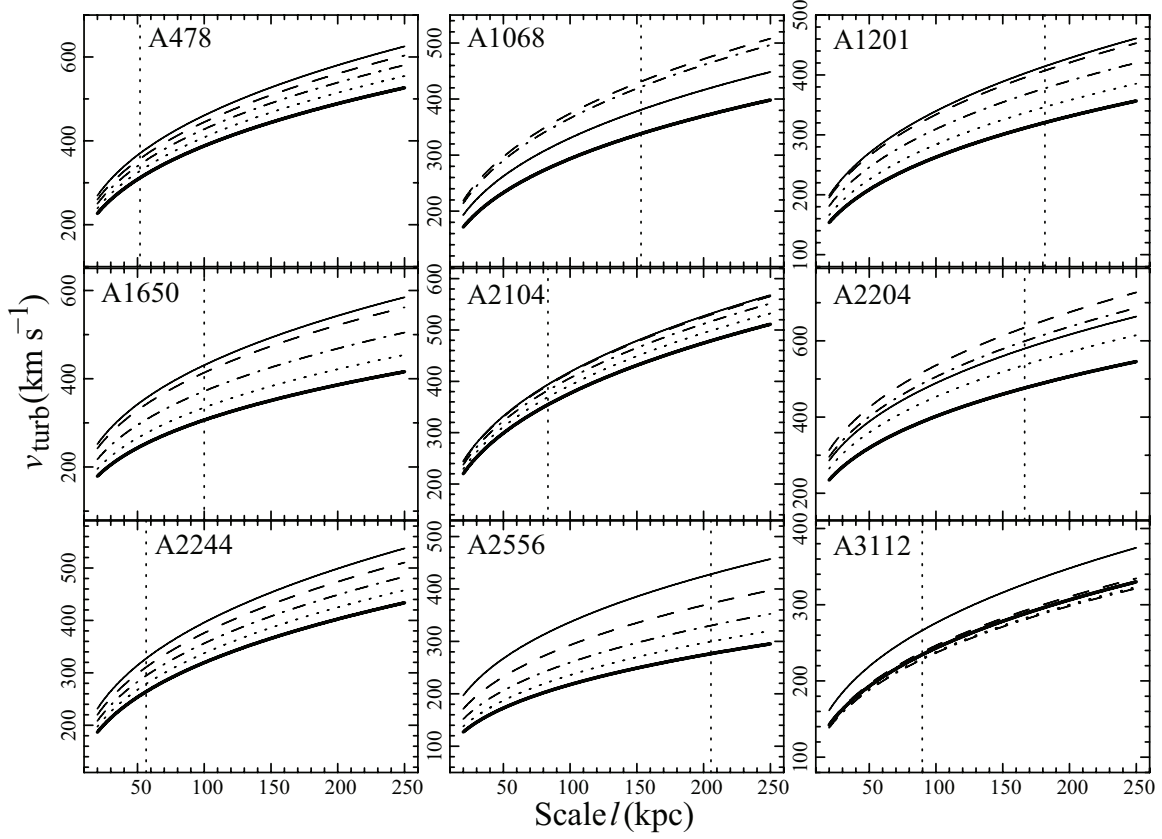


Fig. 7.— Turbulence velocities v_{turb} as a function of turbulence length scales l , which are plotted for the radius of 100 (solid), 125 (dash), 150 (dash dot), 175 (dot), and 200 (thick solid) h_{70}^{-1} kpc, respectively. The vertical lines mark the turnover points obtained in the wavelet spectra (§4.1 and Fig. 5).